On Multiwavelet-Based Finite-Element Method

Guangwen (George) W. Pan, *Senior Member, IEEE*, Ke Wang, and Barry K. Gilbert, *Fellow, IEEE*

***Abstract*—A new approach of using multiwavelets in the finite-element method for electromagnetic-wave problems is presented for the first time. In this approach, the multiscalets are employed as the basis functions. Due to the smoothness, completeness, compact support, and interpolation property of the multiscalets, in terms of the basis function and its derivatives, fast convergence in approximating a function is achieved. The new basis functions are $\in C^1$, i.e., the first derivatives of the bases are continuous on the connecting nodes. Thus, the divergence-free condition is satisfied at the end points. The multiscalets, along with their derivatives, are orthonormal in the discrete sampling nodes. Therefore, no coupled system of equations in terms of the function and its derivative is involved, resulting in a simple and efficient algorithm. Numerical results demonstrate the high efficiency and accuracy of the new method. For a partially loaded waveguide problem, we have achieved a factor of 16 in memory reduction and 435 in CPU speedup over the linear edge-element method.**

***Index Terms*—Compact support, finite-element method (FEM), interpolation, multiresolution analysis (MRA), multiwavelets, propagation modes, regularity, splines, waveguide.**

I. Introduction

THE edge-element method (EEM) is a popular and powerful numerical approach in computational electromagnetics [1]–[3]. It allows the normal component of the vector field to be discontinuous across the adjacent elements and handles field singularity better than the node-based finite-element method (FEM) [4], [5]. While higher order basis functions in the EEM improve numerical accuracy and convergence (in terms of discretization size), they increased the complexity of the algorithm and bandwidth of the system matrix dramatically. The Lagrange-based interpolation matches the function being approximated at the discrete points (nodes) by linear, quadratic, or cubic polynomials, depending on the interpolation order. Nonetheless, the slope (derivative) and curvature (second derivative) of the function have never been matched at the nodes, regardless of the order of the polynomials.

Attempts were made to address the slope by using the splines because of the short support and nice features of the splines [6]. Unfortunately, simultaneous system equations in terms of the function and its derivative values must be solved in order to employ the splines. This complicity has rendered the interpolatory spline unpopular in the FEM.

Recently, advances in wavelets have opened an opportunity to reconsider the problem. The extracting features of standard (scalar) wavelets are orthogonality, vanishing moments, compact support, multiresolution analysis (MRA), regularity, and symmetry. However, it was rigorously proven by Daubechies [7] that standard wavelets cannot simultaneously possess compact support, symmetry, continuity, and orthogonality. In addition, most orthogonal wavelets (except the Haar wavelets) do not have explicit expressions in the time (spatial) domain. Therefore, it is difficult to incorporate wavelets into the FEM. Multiwavelets extended the scalar dilation equation into the vector–matrix form. As a result, more flexibilities are offered by the multiwavelets, i.e., to have simultaneously compact support, MRA, interpolation, orthogonality, and symmetry/antisymmetry, and even explicit expressions.

In this paper, we follow the finite-element formulation, but use multiwavelets as the basis functions to replace the traditional linear or higher order Lagrange interpolation shape functions. We employ the canonical multiwavelets developed by Strela and Strang [9], with the support of $[0, 2]$. They are smooth, interpolating, complete, and compactly supported. For a multiscaling function (we use scalet to be a counterpart of wavelet), the function, its first, second, and third derivatives, are mutually uncoupled, allowing the development of a simple and efficient Galerkin-type algorithm. Under the same partitioning, the nonzero entries in the corresponding system matrix of the multiwavelet FEM is roughly twice that of the linear FEM. The multiwavelet basis matches a function and its slope values when multiplicity $r = 2$, or matches the function, slope, and the curvature if multiplicity $r = 3$. Such a high fidelity in approximation leads to a fast convergence, which can be seen from Taylor's expansion in terms of $|x - x_0| \leq \Delta x$, the interval size. Hence, the multiwavelet discretization may be much coarser, yet produces the same numerical precision as the linear EEM with much finer mesh size. It is noticed that enforcement of higher order derivative continuities worsens the resulting system matrix slightly, provided the basis functions are properly scaled. In this paper, only $r = 2$ is implemented. Numerical examples of one-dimensional (1-D) Sturm–Liouville problem and two-dimensional (2-D) partially loaded waveguide problem demonstrate the high efficiency and accuracy of the proposed method.

II. Orthogonal Multiwavelets

A. Basic Theory

Basic theory of orthogonal multiwavelets can be found in many mathematical papers [9]–[11]. However, for readers without mathematical sophistication, it is not a trivial task to comprehend the arcane concepts and convert them into meaningful and useful engineering tools. In this section, we briefly quote basic multiwavelet principles that are used to construct and facilitate the orthogonal multiwavelets. The multiscalets $\phi_0(t), \phi_1(t), \ldots, \phi_{r-1}(t)$ are polynomials of degree $2r - 1$ on $[0, 1]$ and $[1, 2]$ and zero elsewhere, with $r - 1$ continuous

Manuscript received September 21, 2001; revised March 15, 2002.

G. W. Pan and K. Wang are with the Department of Electrical Engineering, Arizona State University, Tempe, AZ 85287 USA.

B. K. Gilbert is with the Mayo Foundation, Rochester, MN 55905 USA.

Digital Object Identifier 10.1109/TMTT.2002.806928

derivatives. They satisfy

$$\Phi(n) = \delta_{1,n} I \tag{1}$$

where

$$\Phi(t) = \begin{bmatrix} \phi_0(t) & \cdots & \phi_0^{(r-1)}(t) \\ \vdots & & \vdots \\ \phi_{r-1}(t) & \cdots & \phi_{r-1}^{(r-1)}(t) \end{bmatrix}$$

$\delta_{0,n}$ = Kronecker delta

I = identity matrix of $r \times r$

r = multiplicity. (2)

The column vector

$$\phi(t) := \left(\phi_0(t) \cdots \phi_{r-1}(t)\right)^T \tag{3}$$

satisfies the matrix dilation equation

$$\phi(t) = \sum_k C_k \phi(2t-k) \tag{4}$$

where the coefficients C_k are matrices of $r \times r$ and are computed in Section II-B. The orthogonal multiwavelets also satisfy the matrix dilation equation

$$\breve{\psi}(t) = \sum_j D_k \phi(2t-k) \tag{5}$$

where the coefficients D_k can be solved in terms of C_k. The detailed discussion can be found in [12]. The multiscalets $\phi(2^j t - k)$ generate subspaces V_j, $j \in Z$ such that

$$\cdots \subset V_{-1} \subset V_0 \subset \cdots V_j \subset \cdots \tag{6}$$

$$\text{closure}\left\{\bigcup_{j=-\infty}^{\infty} V_j\right\} = L^2(R) \qquad \bigcap_{j=-\infty}^{\infty} V_j = 0. \tag{7}$$

The multiwavelets $\breve{\psi}(t)$ and their translates $\breve{\psi}(t-k)$ are linearly independent and create a basis of the subspace W_0 such that

$$V_1 = V_0 \oplus W_0. \tag{8}$$

It follows from (6) to (8) that

$$L^2(R) = \bigoplus_{j=-\infty}^{\infty} W_j. \tag{9}$$

These properties are referred to as the MRA, the same as the scalar wavelet case. In this paper, only the multiscalets are employed.

If we take a close look at (1), we find that

$$\Phi(1) = \begin{bmatrix} \phi_0(1) & \phi_0'(1) & \cdots & \phi_0^{(r-1)}(1) \\ \phi_1(1) & \phi_0'(1) & \cdots & \phi_1^{(r-1)}(1) \\ \cdots & \cdots & \cdots & \cdots \\ \phi_{r-1}(1) & \phi_{r-1}'(1) & \cdots & \phi_{r-1}^{(r-1)}(1) \end{bmatrix} = \begin{bmatrix} 1 & 0 & \cdots & 0 \\ 0 & 1 & \cdots & 0 \\ \cdots & & \cdots & \\ 0 & 0 & \cdots & 1 \end{bmatrix}.$$

Explicitly, it states that $\phi_0(t)$ interpolates at the sampling point (integer) $t = 1$, but assumes 0 at other sampling points $t = 0$, $t = 2$. The derivatives $\phi_0^{(\ell)}(t)$, $\ell = 1, 2, \ldots, r-1$ are zero at all integer sampling points. Similarly, $\phi_1'(t)$ interpolates at integer point $t = 1$, but assumes zero elsewhere for any derivatives other than 1. In general,

$$\phi_i^{(j)}(m) = \delta_{i,j}\delta_{1,m}, \qquad i, j = 0, 1, \ldots, r-1. \tag{10}$$

While spline interpolation fits a set of function values by solving a coupled linear system, the property (10) of the multiwavelets provides interpolation that is completely uncoupled. $\phi_i(t)$, $i = 0, \ldots, r-1$ will be employed in the finite element as the shape functions.

B. Construction of Multiscalets

It can be derived [10] that the coefficients matrices in (4) are

$$C_0 = \Phi\left(\frac{1}{2}\right)\Lambda$$

$$C_1 = \Phi\left(\frac{1}{2}\right)\Lambda = I\Lambda = \Lambda = \text{diag}\left\{1, \frac{1}{2}, \ldots, \left(\frac{1}{2}\right)^{r-1}\right\}$$

$$C_2 = \Phi\left(\frac{3}{2}\right)\Lambda. \tag{11}$$

Matrices C_2 and C_0 are related by

$$C_0 = SC_2S^{-1} \tag{12}$$

with

$$S = S^{-1} = \begin{bmatrix} 1 & & & \\ & (-1) & & \\ & & \cdots & \\ & & & (-1)^{r-1} \end{bmatrix}. \tag{13}$$

Matrix C_2 is given by

$$C_2 = U^{-1}\Gamma U \tag{14}$$

where

$$\Gamma = \text{diag}\left\{\left(\frac{1}{2}\right)^r, \left(\frac{1}{2}\right)^{r+1}, \ldots, \left(\frac{1}{2}\right)^{2r-1}\right\} \tag{15}$$

and

$$[U]_{mn} = (-1)^{r+m-n}\frac{(r+m-1)!}{(r+m-n)!}. \tag{16}$$

For the piecewise cubic case, i.e., $r = 2$,

$$\Gamma = \begin{bmatrix} \frac{1}{4} & 0 \\ 0 & \frac{1}{8} \end{bmatrix} \quad U = \begin{bmatrix} \frac{2!}{2!} & -\frac{2!}{1!} \\ -\frac{3!}{3!} & \frac{3!}{2!} \end{bmatrix} = \begin{bmatrix} 1 & -2 \\ -1 & 3 \end{bmatrix}.$$

Hence,

$$C_2 = U^{-1}\Gamma U = \begin{bmatrix} \frac{1}{2} & -\frac{3}{4} \\ \frac{1}{8} & -\frac{1}{8} \end{bmatrix}$$

$$C_0 = SC_2S^{-1} = \begin{bmatrix} \frac{1}{2} & \frac{3}{4} \\ -\frac{1}{8} & -\frac{1}{8} \end{bmatrix}$$

and C_1 was given in (11) as

$$C_1 = \begin{bmatrix} 1 & 0 \\ 0 & \frac{1}{2} \end{bmatrix}.$$

Since the support of $\phi(t)$ is $[0, 2]$, the nonzero coefficients (called low-pass filters in wavelet literature) are only C_0, C_1, and C_2. Following the construction of the Daubechies scalets [7], the multiscalets $\phi_0(t)$ and $\phi_1(t)$ can be built by a simple iteration program or an eigenvalue algorithm called the cascade method. While the Daubechies scalets constructed by the aforementioned methods do not have analytical expressions, the multiscalets do have explicit formulas. It was found that, for $r = 2$,

$$t \in [0, 1] \begin{cases} \phi_0(t) = 3t^2 - 2t^3 \\ \phi_1(t) = t^3 - t^2 \end{cases} \tag{17}$$

and

$$t \in [1, 2] \begin{cases} \phi_0(t) = \phi_0(2 - t) \\ \phi_1(t) = -\phi_1(2 - t). \end{cases} \tag{18}$$

It may be verified easily that

$$\Phi(t)|_{t=1} = \begin{bmatrix} \phi_0(t) & \phi_0'(t) \\ \phi_1(t) & \phi_1'(t) \end{bmatrix}_{t=1} = \begin{bmatrix} 1 & 0 \\ 0 & 1 \end{bmatrix}.$$

The curves of $\phi_0(t)$ and $\phi_1(t)$ obtained by an iteration method and by explicit expressions are plotted in Fig. 1. It can be seen that $\phi_0(t)$ and $\phi_1(t)$ are symmetric and antisymmetric about $t = 1$, respectively.

For higher values of multiplicity r,

$$\phi_j(2 - t) = (-1)^j \phi_j(t), \qquad j = 0, \ldots, r - 1. \tag{19}$$

In case of $r = 3$,

$$C_0 = \begin{bmatrix} \frac{1}{2} & \frac{15}{16} & 0 \\ -\frac{5}{32} & -\frac{7}{32} & \frac{3}{8} \\ \frac{1}{64} & \frac{1}{64} & -\frac{1}{16} \end{bmatrix}$$

$$C_1 = \begin{bmatrix} 1 & 0 & 0 \\ 0 & \frac{1}{2} & 0 \\ 0 & 0 & \frac{1}{4} \end{bmatrix}$$

$$C_2 = \begin{bmatrix} \frac{1}{2} & -\frac{15}{16} & 0 \\ \frac{5}{32} & -\frac{7}{32} & -\frac{3}{8} \\ \frac{1}{64} & -\frac{1}{64} & -\frac{1}{16} \end{bmatrix}.$$

The curves of $\phi_0(t)$, $\phi_1(t)$ and $\phi_2(t)$ are plotted in Fig. 2. The explicit polynomials of $\phi_0(t)$, $\phi_1(t)$ and $\phi_2(t)$ are

$$\phi_0(t) = 6t^5 - 15t^4 + 10t^3$$

$$\phi_1(t) = -3t^5 + 7t^4 - 4t^3$$

$$\phi_2(t) = \frac{1}{2}t^5 - t^4 + \frac{1}{2}t^3$$

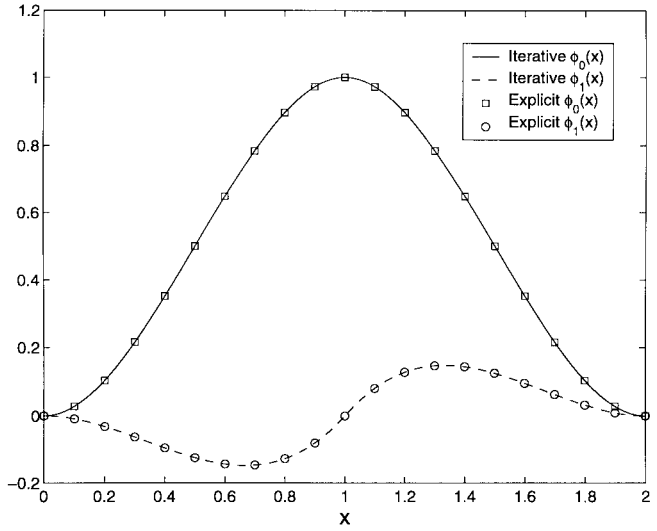

Fig. 1. Multiwavelets of $r = 2$.

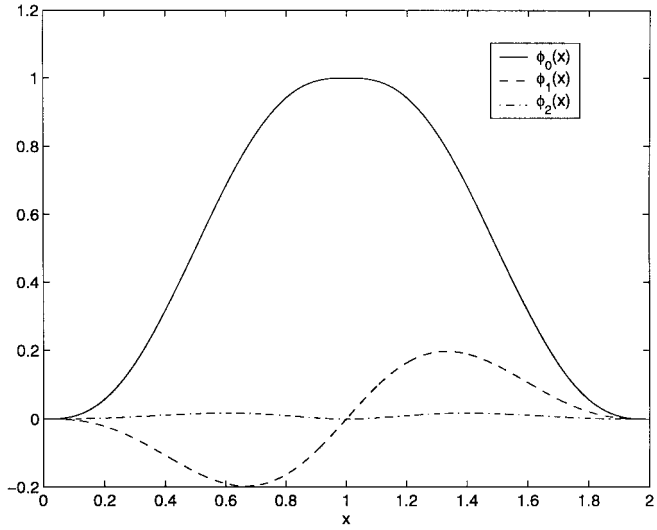

Fig. 2. Multiwavelets of $r = 3$.

on the interval $[0, 1]$. Using the symmetry/antisymmetry, one can obtain the closed-form expressions on the interval $[1, 2]$. General expressions of multiscalets with arbitrary r can be found in [12].

III. Formulation of the Problem

A. 1-D Case

A typical boundary-value problem can be defined by a governing differential equation in a domain Ω

$$L\phi = f \tag{20}$$

together with boundary conditions on the boundary Ω that encloses the domain. Here, L is a differential operator, f is the excitation, and ϕ is the unknown function.

In the FEM, the first step is to divide the computational domain into small subdomains, which are called elements. The second step is to select the interpolation functions and then representing the unknown function in each subdomain with the interpolation functions. The third and fourth steps are to formulate

the system equations and to solve the system equations. In the simplest case, the Lagrange linear interpolation functions are employed.

An improvement of the FEM is to use high-order interpolation functions. However, the derivatives of the unknown function at the connecting nodes of subdomains are still discontinuous. To overcome this drawback, multiwavelet basis functions are adopted. These basis functions are of high-order interpolation functions

$$\begin{aligned} N_1^e &= 3\left(\frac{x_2^e - x}{l_e}\right)^2 - 2\left(\frac{x_2^e - x}{l_e}\right)^3 \\ N_2^e &= 3\left(\frac{x - x_1^e}{l_e}\right)^2 - 2\left(\frac{x - x_1^e}{l_e}\right)^3 \\ D_1^e &= -\left[\left(\frac{x_2^e - x}{l_e}\right)^3 - \left(\frac{x_2^e - x}{l_e}\right)^2\right] \cdot l_e \\ D_2^e &= \left[\left(\frac{x - x_1^e}{l_e}\right)^3 - \left(\frac{x - x_1^e}{l_e}\right)^2\right] \cdot l_e \end{aligned} \tag{21}$$

where the superscript e stands for elements. Fig. 3 depicts the four basis functions.

By comparing (21) against (17) and (18), one finds that N_2 is ϕ_0, given in (17), but shifted by x_1^e and scaled by l_e. N_1 is ϕ_0, given in (18), but shifted by x_2^e and scaled by l_e. Similarly, D_1 and D_2 are the shifted and scaled versions of ϕ_1.

A feature of the multiwavelets basis is that the values of D vanish at the two nodes x_1^e and x_2^e, while the derivatives of N vanish at the two nodes. Therefore, the unknown function can be written as

$$\phi^e(x) = \sum_{j=1}^{2} \phi_j^e N_j^e(x) + \phi_j'^e D_j^e(x) \tag{22}$$

$$\phi'^e(x) = \sum_{j=1}^{2} \phi_j^e N_j'^e(x) + \phi_j'^e D_j'^e(x). \tag{23}$$

Let us consider a 1-D Sturm–Liouville problem

$$-\frac{d}{dx}\left(\alpha \frac{d\phi}{dx}\right) + \beta\phi = f. \tag{24}$$

The Galerkin method produces the following formulas:

$$\begin{aligned} &\left\langle N_i^e, -\frac{d}{dx}\left(\alpha \frac{d\phi}{dx}\right) + \beta\phi - f \right\rangle \\ &= \int_{x_1^e}^{x_2^e} N_i^e \left[-\frac{d}{dx}\left(\alpha \frac{d\phi}{dx}\right) + \beta\phi\right] dx - \int_{x_1^e}^{x_2^e} N_i^e f\, dx \\ &= \int_{x_1^e}^{x_2^e} \left(\alpha \frac{dN_i^e}{dx}\frac{d\phi}{dx} + \beta N_i^e \phi\right) dx \\ &\quad - \int_{x_1^e}^{x_2^e} N_i^e f\, dx - \alpha N_i^e \left.\frac{d\phi}{dx}\right|_{x_1^e}^{x_2^e} \\ &= \sum_{j=1}^{2} \phi_j^e \underbrace{\int_{x_1^e}^{x_2^e} (\alpha N_i'^e N_j'^e + \beta N_i^e N_j^e)\, dx}_{K_{ij}} \\ &\quad + \phi_j'^e \underbrace{\int_{x_1^e}^{x_2^e} (\alpha N_i'^e D_j'^e + \beta N_i^e D_j^e)\, dx}_{L_{ij}} \\ &\quad - \int_{x_1^e}^{x_2^e} N_i^e f dx - \underbrace{\alpha N_i^e (\phi_2'^e - \phi_1'^e)}_{\text{boundary}} \end{aligned} \tag{25}$$

and

$$\begin{aligned} &\left\langle D_i^e, -\frac{d}{dx}\left(\alpha \frac{d\phi}{dx}\right) + \beta\phi - f \right\rangle \\ &= \int_{x_1^e}^{x_2^e} D_i^e \left[-\frac{d}{dx}\left(\alpha \frac{d\phi}{dx}\right) + \beta\phi\right] dx - \int_{x_1^e}^{x_2^e} D_i^e f\, dx \\ &= \int_{x_1^e}^{x_2^e} \left(\alpha \frac{dD_i^e}{dx}\frac{d\phi}{dx} + \beta D_i^e \phi\right) dx \\ &\quad - \int_{x_1^e}^{x_2^e} D_i^e f\, dx - \alpha D_i^e \left.\frac{d\phi}{dx}\right|_{x_1^e}^{x_2^e} \\ &= \sum_{j=1}^{2} \phi_j^e \underbrace{\int_{x_1^e}^{x_2^e} (\alpha D_i'^e N_j'^e + \beta D_i^e N_j^e)\, dx}_{P_{ij}} \\ &\quad + \phi_j'^e \underbrace{\int_{x_1^e}^{x_2^e} (\alpha D_i'^e D_j'^e + \beta D_i^e D_j^e)\, dx}_{Q_{ij}} \\ &\quad - \int_{x_1^e}^{x_2^e} D_i^e f\, dx - \underbrace{\alpha D_i^e (\phi_2'^e - \phi_1'^e)}_{=0}. \end{aligned} \tag{26}$$

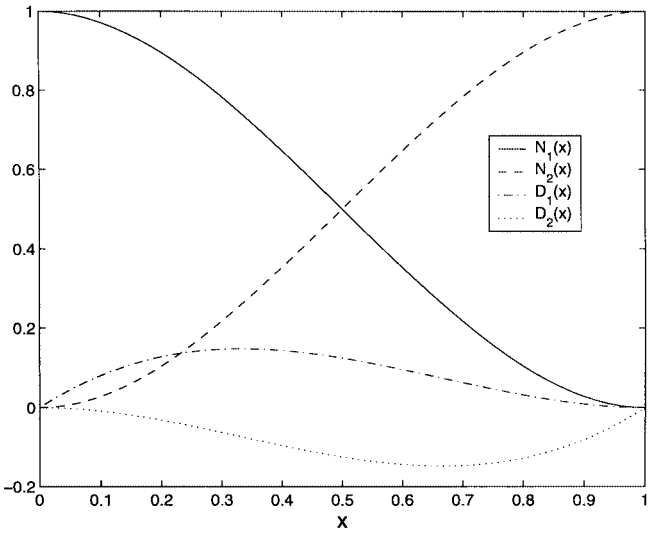

Fig. 3. Four basis functions.

Finally , we arrive at a system equation of the problem

$$\begin{bmatrix} K & L \\ P & Q \end{bmatrix} \begin{bmatrix} \phi \\ \phi' \end{bmatrix} = \begin{bmatrix} g \\ h \end{bmatrix}. \tag{27}$$

In the above equation,

$$K_{ij} = \int_{x_1^e}^{x_2^e} (\alpha N_i'^e N_j'^e + \beta N_i^e N_j^e)\, dx$$

$$L_{ij} = \int_{x_1^e}^{x_2^e} (\alpha N_i'^e D_j'^e + \beta N_i^e D_j^e)\, dx$$

$$P_{ij} = \int_{x_1^e}^{x_2^e} (\alpha D_i'^e N_j'^e + \beta D_i^e N_j^e)\, dx$$

$$Q_{ij} = \int_{x_1^e}^{x_2^e} (\alpha D_i'^e D_j'^e + \beta D_i^e D_j^e)\, dx$$

$$g_i^e = \int_{x_1^e}^{x_2^e} N_i^e f\, dx$$

$$h_i^e = \int_{x_1^e}^{x_2^e} D_i^e f\, dx. \tag{28}$$

B. 2-D Case

The 2-D waveguide problem is considered here. The boundary-value problem in the full-wave analysis of an inhomogeneously filled waveguide is defined by the vector-wave equation

$$\nabla \times \left(\frac{1}{\mu_r} \nabla \times \mathbf{E}\right) - k_0^2 \epsilon_r \mathbf{E} = 0 \text{ in } \Omega \tag{29}$$

with the boundary conditions

$$\hat{n} \times \mathbf{E} = 0 \text{ on } \Gamma_1$$
$$\hat{n} \times (\nabla \times \mathbf{E}) = 0 \text{ on } \Gamma_2. \tag{30}$$

In the previous equations, Ω denotes the cross section of the structure whose boundary is comprised by the electrical wall Γ_1 and the magnetic wall Γ_2. The equivalent variational problem with real ϵ_r and μ_r is given by

$$\begin{cases} \delta F(\mathbf{E}) = 0 \\ \hat{n} \times \mathbf{E} = 0 \text{ on } \Gamma_1 \end{cases} \tag{31}$$

where

$$F(\mathbf{E}) = \frac{1}{2} \iint_\Omega \left[\frac{1}{\mu_r} (\nabla \times \mathbf{E}) \cdot (\nabla \times \mathbf{E})^* - k_0^2 \epsilon_r \mathbf{E} \cdot \mathbf{E}^*\right] d\Omega. \tag{32}$$

Assuming a known z-dependence of $\mathbf{E}(x, y, z) = \mathbf{E}(x, y) e^{-jk_z z}$, the functional can be written as

$$F(\mathbf{E}) = \frac{1}{2} \iint_\Omega \left[\frac{1}{\mu_r} (\nabla_t \times \mathbf{E}_t) \cdot (\nabla_t \times \mathbf{E}_t)^* - k_0^2 \epsilon_r \mathbf{E}_t \cdot \mathbf{E}_t^* + \frac{1}{\mu_r} (\nabla_t E_z + jk_z \mathbf{E}_t) \cdot (\nabla_t E_z + jk_z \mathbf{E}_t)^*\right] d\Omega.$$

The functional can be discretized to yield an eigenvalue system that can be solved for k_0^2 for a given k_z. However, in engineering practice, it is usually preferred to specify the operating frequency, then solve for propagation constant k_z.

To alleviate the difficulty, the following transformation is introduced [8]:

$$\mathbf{e}_t = k_z \mathbf{E}_t \quad e_z = -jE_z.$$

The normalized version of the functional is

$$F(\mathbf{e}) = \frac{1}{2} \iint_\Omega \left\{ \frac{1}{\mu_r} (\nabla_t \times \mathbf{e}_t) \cdot (\nabla_t \times \mathbf{e}_t)^* - k_0^2 \epsilon_r \mathbf{e}_t \cdot \mathbf{e}_t^* + k_z^2 \left[\frac{1}{\mu_r} (\nabla_t e_z + \mathbf{e}_t) \cdot (\nabla_t e_z + \mathbf{e}_t)^* - k_0^2 \epsilon_r e_z e_z^*\right]\right\} d\Omega.$$

Apparently, the eigenvalue equation of discretization of this functional for a given k_0 will result in a system with k_z^2 as its eigenvalue. To this end, the cross-sectional area Ω is subdivided into small rectangular or triangular elements. Within each element, the vector field can be expanded as

$$\mathbf{e}_t^e = \sum_{i=1}^n \mathbf{N}_i^e e_{ti}^e = \{\mathbf{N}^e\}^T \{e_t^e\} = \{e_t^e\}^T \{\mathbf{N}^e\} \tag{33}$$

and

$$e_z^e = \sum_{i=1}^n N_i^e e_{zi}^e = \{N^e\}^T \{e_z^e\} = \{e_z^e\}^T \{N^e\} \tag{34}$$

where $\mathbf{N}_i^e$ and N_i^e are vector and scalar interpolation functions, respectively.

The functional can then be discretized as

$$F = \frac{1}{2} \sum_{e=1}^M \left(\{e_t^e\}^T [A_{tt}^e] \{e_t^e\}^* + k_z^2 \begin{Bmatrix} e_t^e \\ e_z^e \end{Bmatrix}^T \cdot \begin{bmatrix} B_{tt}^e B_{tz}^e \\ B_{zt}^e B_{zz}^e \end{bmatrix} \begin{Bmatrix} e_t^e \\ e_z^e \end{Bmatrix}^* \right) \tag{35}$$

where A_{tt}^e, B_{tt}^e, B_{tz}^e, B_{zt}^e, and B_{zz}^e are all integrals in the corresponding elements, which can be evaluated analytically.

Adding all elements into a global matrix, we obtain the system matrix of

$$[A_{tt}]\{e_t\} = k_z^2 [B_{tt}'] \{e_t\} \tag{36}$$

where

$$[B_{tt}'] = [B_{tz}][B_{zz}]^{-1}[B_{zt}] - [B_{tt}].$$

Traditionally, one employs the linear interpolation functions

$$\mathbf{N}_1^e = \left(\frac{y_2^e - y}{l_y}\right) \hat{x}$$
$$N_1^e = \frac{(x_2^e - x)(y_2^e - y)}{l_x l_y}$$
$$\mathbf{N}_2^e = \left(\frac{x - x_1^e}{l_x}\right) \hat{y}$$
$$N_2^e = \frac{(x - x_1^e)(y_2^e - y)}{l_x l_y}$$
$$\mathbf{N}_3^e = \left(\frac{y - y_1^e}{l_y}\right) \hat{x}$$
$$N_3^e = \frac{(x - x_1^e)(y - y_1^e)}{l_x l_y}$$
$$\mathbf{N}_4^e = \left(\frac{x_2^e - x}{l_x}\right) \hat{y}$$
$$N_4^e = \frac{(x_2^e - x)(y - y_1^e)}{l_x l_y}. \tag{37}$$

Here, we use multiwavelet interpolation functions as the edge bases

$$\mathbf{N}_1^e = \left[3\left(\frac{y_2^e - y}{l_y}\right)^2 - 2\left(\frac{y_2^e - y}{l_y}\right)^3\right]\hat{x}$$

$$\mathbf{N}_2^e = \left[3\left(\frac{x - x_1^e}{l_x}\right)^2 - 2\left(\frac{x - x_1^e}{l_x}\right)^3\right]\hat{y}$$

$$\mathbf{N}_3^e = \left[3\left(\frac{y - y_1^e}{l_y}\right)^2 - 2\left(\frac{y - y_1^e}{l_y}\right)^3\right]\hat{x}$$

$$\mathbf{N}_4^e = \left[3\left(\frac{x_2^e - x}{l_x}\right)^2 - 2\left(\frac{x_2^e - x}{l_x}\right)^3\right]\hat{y}$$

$$\mathbf{N}_5^e = -l_y\left[\left(\frac{y_2^e - y}{l_y}\right)^3 - \left(\frac{y_2^e - y}{l_y}\right)^2\right]\hat{x}$$

$$\mathbf{N}_6^e = l_x\left[\left(\frac{x - x_1^e}{l_x}\right)^3 - \left(\frac{x - x_1^e}{l_x}\right)^2\right]\hat{y}$$

$$\mathbf{N}_7^e = l_y\left[\left(\frac{y - y_1^e}{l_y}\right)^3 - \left(\frac{y - y_1^e}{l_y}\right)^2\right]\hat{x}$$

$$\mathbf{N}_8^e = -l_x\left[\left(\frac{x_2^e - x}{l_x}\right)^3 - \left(\frac{x_2^e - x}{l_x}\right)^2\right]\hat{y} \tag{38}$$

where the last four interpolation functions are the derivative bases denoted as D_j^e in (22) and (23). The reason we changed notation is to have a compact expression of (39), as shown below. The interpolation functions for the z-component remain unchanged, and the transverse fields are written as

$$\mathbf{e}_t^e = \sum_{i=1}^{8} \mathbf{N}_i^e e_{ti}^e = \{\mathbf{N}^e\}^T\{e_t^e\} \tag{39}$$

where

$$\{e_t^e\} = \{e_{t1}^e, e_{t2}^e, e_{t3}^e, e_{t4}^e, e_{t1}'^e, e_{t2}'^e, e_{t3}'^e, e_{t4}'^e\}^T. \tag{40}$$

IV. Numerical Results

Example 1: For a 1-D case, we choose a simple problem

$$\frac{d^2\phi}{dx^2} = x + 1, \qquad 0 < x < 1$$

$$\phi|_{x=0} = 0$$

$$\phi|_{x=1} = 1.$$

The analytical solution is given in [8] as

$$\phi(x) = \frac{1}{6}x^3 + \frac{1}{2}x^2 + \frac{1}{3}x.$$

The comparison of the analytical solution with the result obtained by a multiwavelets-based FEM is plotted in Fig. 4. From this figure, the numerical solution matches the function and its derivative values very well.

Example 2: Dispersion characteristics of a partially loaded waveguide, as shown in Fig. 5, are computed to test the multiwavelets-based EEM. The results are plotted in Fig. 6. As a comparison, the first six propagation modes obtained by using the traditional linear EEM are plotted in Fig. 7.

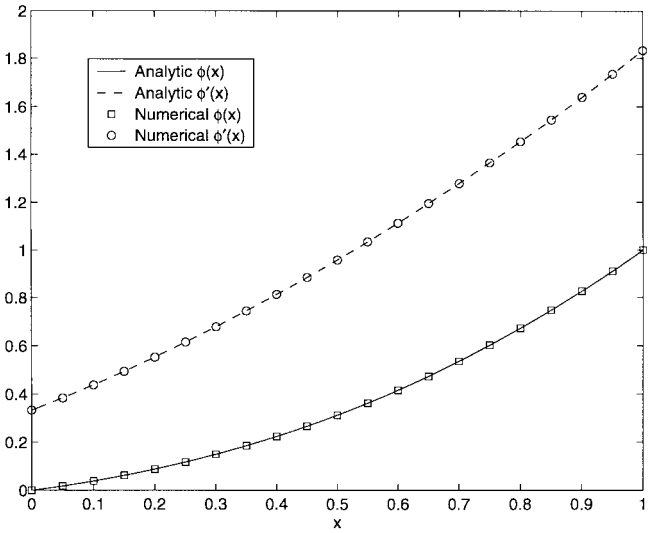

Fig. 4. Multiwavelets-based FEM in a 1-D case.

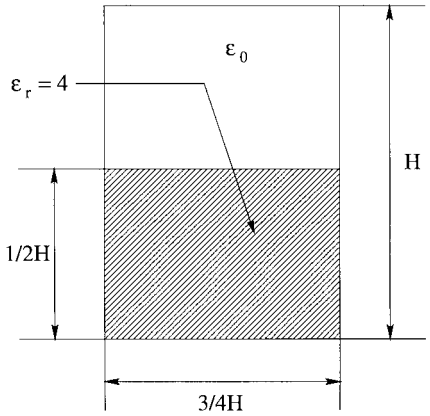

Fig. 5. Configuration of a partially loaded waveguide.

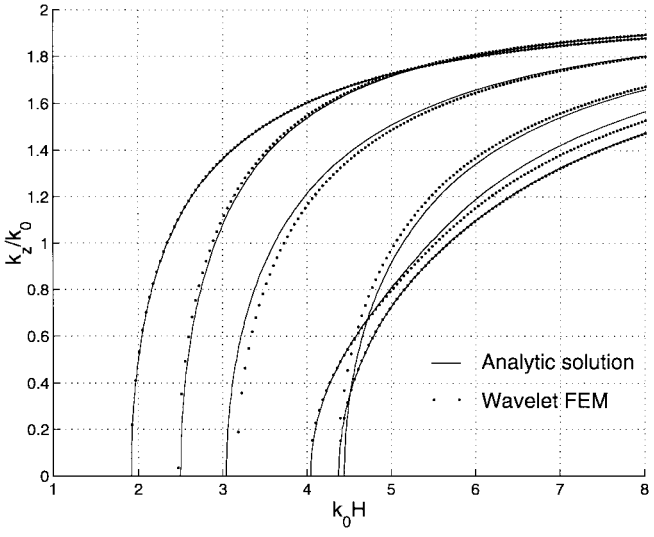

Fig. 6. Results obtained by the multiwavelet FEM (4 × 4 elements).

While the wavelet FEM faithfully predicts the dominating mode, the linear FEM demonstrates substantial errors on the dominating mode. For the higher order modes, the wavelet FEM closely follows the trend of the analytic solutions. In contrast,

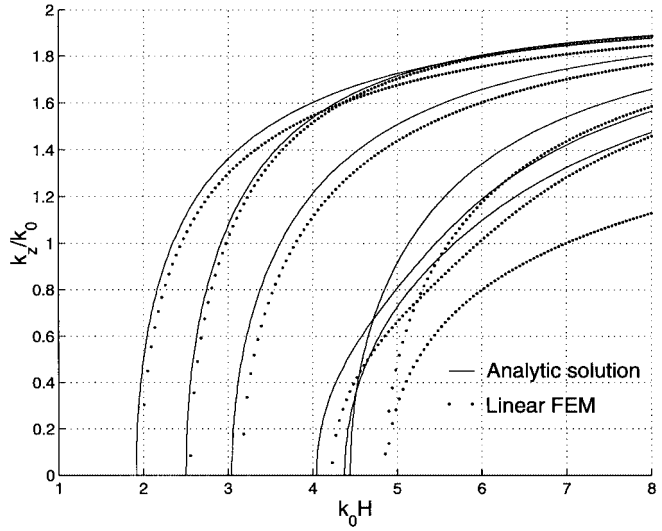

Fig. 7. Results obtained by the linear FEM (4 × 4 elements).

TABLE I
L^2 PERFORMANCE COMPARISON FOR THE DOMINATING MODE

Elements	L2 error	CPU time on DEC Alpha 433 (161 frequency points)
Multiwavelets based FEM		
4 x 4	0.064%	24s
Linear based FEM		
4 x 4	12.9%	1.7s
6 x 6	8.73%	20s
8 x 8	8.23%	117s
10 x 10	3.46%	486s
12 x 12	2.21%	1539s
16 x 16	1.15%	10459s

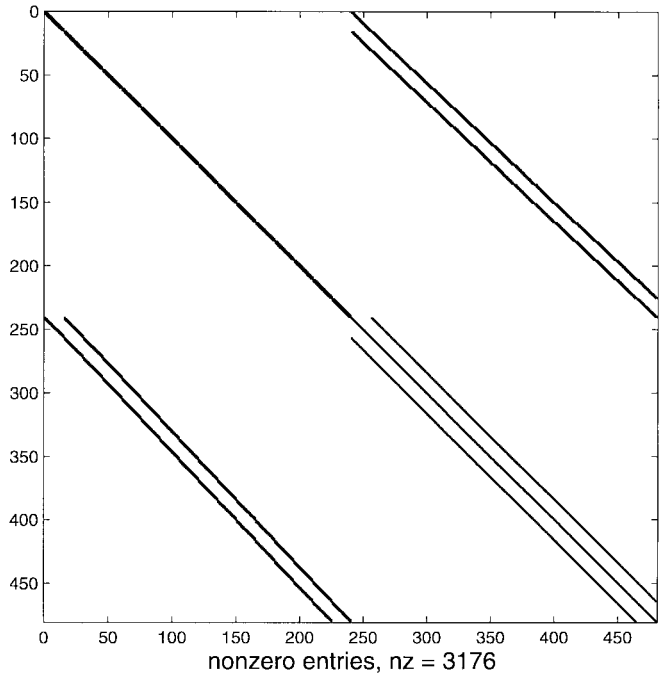

Fig. 8. Linear EEM matrix from an inhomogeneous waveguide with 16 × 16 elements.

the linear FEM lost tracking of the fourth to sixth modes. To compare the two approaches quantitatively, we created Table I.

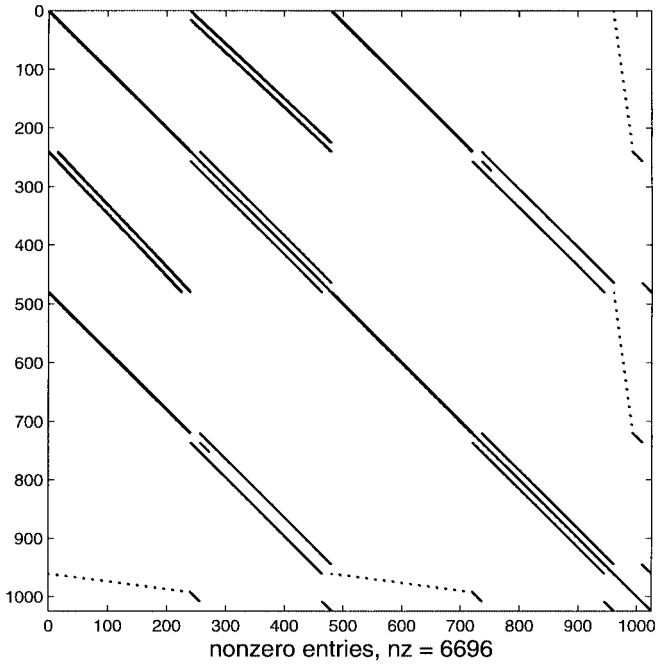

Fig. 9. Multiwavelet EEM matrix from an inhomogeneous waveguide with 16 × 16 elements.

It can be clearly seen that, in terms of the L^2 error, the wavelet FEM with 4 × 4 elements performs better than the linear FEM of 16 × 16 elements. This result reveals a memory saving of 16 and a CPU time cut of 435.

Interestingly enough, under the same discretization, the matrix size of the multiwavelet EEM is roughly 2 × 2 times that of the linear EEM. This is due to the fact that we add the derivative bases into the multiwavelet EEM in addition to the function bases. However, the nonzero entries in the multiwavelet matrix only increased approximately twice. Figs. 8 and 9 illustrate the matrix pattern and nonzero elements from the inhomogeneous waveguide with 16 × 16 elements. Notice that the multiwavelet solution in Table I never used the 16 × 16 division since the 4 × 4 multiwavelet scheme has already had superior performance to that of the 16 × 16 linear FEM.

V. CONCLUSION

In this paper, the multiwavelet scaling functions have been constructed and applied to the 1-D and 2-D finite-element formulation. As a result of the smoothness, interpolatory property, orthogonality, compact support, and symmetry/antisymmetry of the multiscalets, fast convergence of the new algorithm has been achieved. This method has yielded enormous savings in computational effort compared to prior methods, and can easily be extended to three-dimensional (3-D) problems using cubic elements.

ACKNOWLEDGMENT

The authors would like to thank Dr. D. Cochran, Defense Science Office of the Defense Advanced Research Projects Agency (DARPA/DSO), Arlington, VA, Dr. C. Hanson, Space Warfare Systems Center Code 80, San Diego, CA, for administrative support and many helpful discussions, Dr. G. Lei

and R. Techentin, Mayo Foundation, Rochetser, MN, and Dr. M. Toupikov, X. Xie and Z. Zhang, Arizona State University, Tempe, for technical assistance.

REFERENCES

[1] R. Graglia, D. Wilton, and A. Peterson, "Higher order interpolatory vector bases for computational electromagnetics," *IEEE Trans. Antennas Propagat.*, vol. 45, pp. 329–342, Mar. 1997.
[2] J. Webb, "Edge elements and what they can do for you," *IEEE Trans. Magn.*, vol. 29, pp. 1460–1465, Mar. 1992.
[3] J. Lee, D.-K. Sun, and Z. Cendes, "Full-wave analysis of dielectric waveguides using tangential vector finite elements," *IEEE Trans. Microwave Theory Tech.*, vol. 39, pp. 1262–1271, Aug. 1991.
[4] J. Tan and G. Pan, "A new edge element analysis of dispersive waveguide structures," *IEEE Trans. Microwave Theory Tech.*, vol. 43, pp. 2600–2607, Nov. 1995.
[5] L. Andersen and J. Volakis, "Development and application of a novel class of hierarchical tangential vector finite elements for electromagnetics," *IEEE Trans. Antennas Propagat.*, vol. 47, pp. 112–120, Jan. 1999.
[6] X. Liang, B. Jian, and G. Ni, "The B-spline finite element method applied to axi-symmetrical and nonlinear field problems," *IEEE Trans. Magn.*, vol. 24, pp. 27–30, Jan. 1988.
[7] I. Daubechies, *Ten Lectures on Wavelets*. Philadelphia, PA: SIAM, 1992, pp. 251–253.
[8] J. Jin, *The Finite Element Method in Electromagnetics*. New York: Wiley, 1993.
[9] V. Strela and G. Strang, "Finite element multiwavelets," in *Approximation Theory, Wavelets and Applications*, ser. NATO Adv. Sci. Instrum. C, Math Phys. Sci. 454. Dordrecht, The Netherlands: Kluwer, 1995.
[10] V. Strela, "Multiwavelets: Theory and applications," Ph.D. dissertation, Dept. Math., Massachusetts Inst. Technol., Cambridge, MA, June 1996.
[11] G. Walter. "Orthogonal finite element multiwavelets," preprints.
[12] G. Pan, *Wavelets in Electromagnetics and Device Modeling.* New York: Wiley, 2003.

Guangwen (George) W. Pan (S'81–M'84–SM'94) received the M.S. and Ph.D. degree in electrical engineering from the University of Kansas, Lawrence, in 1982 and 1984, respectively.

He was a Post-Doctoral Fellow with the University of Texas (1984–1985), an Engineer with the Mayo Foundation (1985–1986), and an Associate Professor with South Dakota State University (1986–1988). From 1988 to 1995, he was with the University of Wisconsin–Milwaukee, where, in 1993, he became a Professor. In 1995, he joined Arizona State University, Tempe, as Professor and Director of the Electric Packaging Laboratory, Electrical Engineering Department. His research area is applied electromagnetics, including packaging, interconnects, and device modeling.

Ke Wang was born in Chongqing, China, in 1972. He received the B.S.E.E. degree from the Nanjing University of Aeronautics and Astronautics, Nanjing, China, in 1993, and the M.S. degree from Sichuan University, Sichuan, China, in 2000, both in electrical engineering, and is currently working toward the Ph.D. degree in electrical engineering at Arizona State University, Tempe.

From 1993 to 1997, he was an Electrical Design Engineer. Since 2000, he has been a Research Associate with the Department of Electrical Engineering, Arizona State University. His current research interests are computational electromagnetics and semiconductor device simulation.

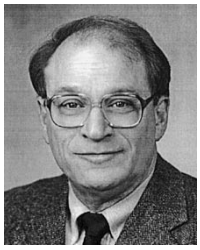

Barry K. Gilbert (S'62–M'70–SM'87–F'98) received the B.S. degree in electrical engineering from Purdue University, West Lafayette, IN, in 1965, and the Ph.D. degree in physiology and biophysics (with minors in electrical engineering and applied mathematics) from the University of Minnesota at Minneapolis–St. Paul, in 1972.

He is currently a Staff Scientist with the Department of Physiology and Biophysics, Mayo Foundation, Rochester, MN, and the Director of the Special-Purpose Processor Development Group, Mayo Foundation (60 full-time staff members). His research interests include the development of algorithms for the real-time analysis of wide-bandwidth image and signal data, the design of specialized signal-processing computers to execute these tasks, the development of computer-aided design (CAD) tools to allow the timely design of high-complexity digital-signal processors, the advancement of high-performance integrated-circuit technologies, such as gallium arsenide, and indium phosphide, which can be used to assemble very high-performance signal processors, and the development of advanced electronic packaging technologies such as multichip modules, which will be capable of supporting digital integrated circuit-based processors operating at gigahertz system clock rates.